ACS APPLIED MATERIALS & INTERFACES

Research Article

www.acsami.org

Fabrication and Characterization of Thin Film Nickel Hydroxide Electrodes for Micropower Applications

Hamid Falahati, Edward Kim, and Dominik P. J. Barz*

Queen's-RMC Fuel Cell Research Centre, Kingston, Ontario K7L 5L9, Canada

ABSTRACT: The utilization of micropower sources is attractive in portable microfluidic devices where only low-power densities and energy contents are required. In this work, we report on the microfabrication of patterned α-$Ni(OH)_2$ films on glass substrates which can be used for rechargeable microbatteries as well as for microcapacitors. A multilayer deposition technique is developed based on e-beam evaporation, ultraviolet lithography, and electroplating/electrodeposition which creates thin-film electrodes that are patterned with arrays of micropillars. The morphology and the structure of the patterned electrode films are characterized by employing field emission scanning electron microscopy. The chemical (elemental) composition is investigated by using X-ray diffraction and X-ray photoelectron spectroscopy. Finally, cyclic voltammetry, electrochemical impedance spectroscopy, and galvanostatic charge/discharge measurements are used to evaluate the electrochemical performance of the patterned thin film electrodes compared to patternless electrodes. We observe that patterning of the electrodes results in significantly improved stability and, thus, longer endurance while good electrochemical performance is maintained.

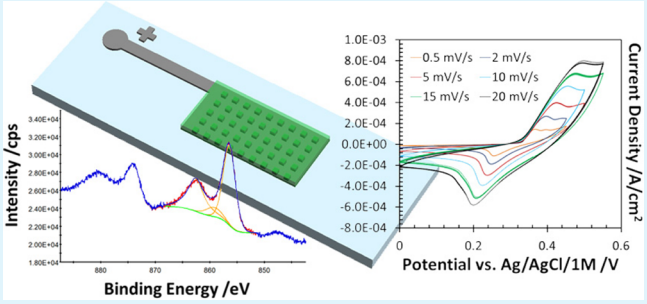

KEYWORDS: *nickel hydroxide, thin-film electrode, multilayer deposition, surface patterning*

1. INTRODUCTION

In the last 2 decades, micro-electro-mechanical systems (MEMS) and especially microfluidic systems have attracted considerable attention since they offer size reduction along with the possibility of integration of several functions in a single unit. The system capabilities usually far exceed those of conventional systems while maintaining the potential of being mass produced at a low cost.[1] Technological microfluidic concepts comprise, for example, Lab-on-a-Chip[2] and Point-of-Care-Testing[3] systems where the typical utilization aims at chemical analytics and medical diagnostics, respectively. However, in almost all microfluidics as well as in other MEMS technologies, the supply of electric power is a barrier to further development since battery miniaturization has not maintained the same pace as the advances in microfabrication methods. That is, the size of a microdevice is often determined by the size of its power supply, and integrating a (macroscopic) power supply within the device structure is often not possible.[4] Typical sub-millimeter-sized sources should produce power in the range of 10^2 to 10^3 μ W cm^{-2} and should have capacities of up to 10^3 μ A h cm^{-2}, at an operating voltage range of 2 to 3 V.[5] Sub-millimeter power sources with such power and energy densities have not yet been developed due to constraints on packaging, fuel storage, fuel delivery, and power generation.[6]

Presently, there are several strategies for the miniaturization of electrical power sources. These include regenerative power technologies that generate power from microphotovoltaic arrays or thermoelectric, electrostatic, and piezoelectric devices.[7,8] In contrast, nonregenerative power supplies have a finite amount, or require a continuous supply of active materials/fuel for power generation, such as microfuel cells[9] and microfluidic fuel cells.[10] Other relevant electrochemical devices are microbatteries where the chemistries are in most cases indistinguishable from conventional batteries, though configurations, material deposition, postprocessing, and packaging methods applicable to macrobatteries are oftentimes not feasible below the centimeter scale. Hence, the resulting microbattery performance does not proportionally scale at such miniature dimensions.[11] Microbatteries typically utilize thin or thick films of electroactive materials which can be either printed or deposited by various techniques such as sol–gel, electrodeposition, physical and chemical vapor deposition, or atomic layer deposition.[12]

Here, micropower sources which utilize nickel hydroxide ($Ni(OH)_2$) films appear promising since they offer well-defined reduction–oxidation (redox) activity, high power/energy density, and good cyclability at low cost. However, the discharge rate and the temperature sensitivity still need to be improved.[13,14] Nevertheless, considerable scientific and technological knowledge of $Ni(OH)_2$ electrodes is available since they have been widely investigated for their utilization in macroscopic batteries, such as nickel/cadmium (Ni/Cd), nickel/metal hydride (Ni/MH), or nickel/zinc (Ni/Zn)[15], as well as in electrochromic devices.[16,17]

Received: March 4, 2015
Accepted: May 22, 2015
Published: May 22, 2015

DOI: 10.1021/acsami.5b01962
ACS Appl. Mater. Interfaces 2015, 7, 12797–12808

The current research on $Ni(OH)_2$ films often aims at (pseudo) electrochemical capacitors including, but not limited to, the work of refs 18−21. For this application, research is also dedicated to the preparation of nanosized particulate $Ni(OH)_2$ which is deposited on carbon nanotubes[22,23] and on nickel foams[24] or clustered to microspheres.[25] Other applications of $Ni(OH)_2$ films aim to increase the electrocatalytic activity and stability of sensors.[26]

The suitability of $Ni(OH)_2$ substrates for electrochemical applications is due to the fact that they can be reversibly converted to nickel oxyhydroxide (NiOOH) as sketched in Figure 1. Generally, $Ni(OH)_2$ has two polymorphic states. The

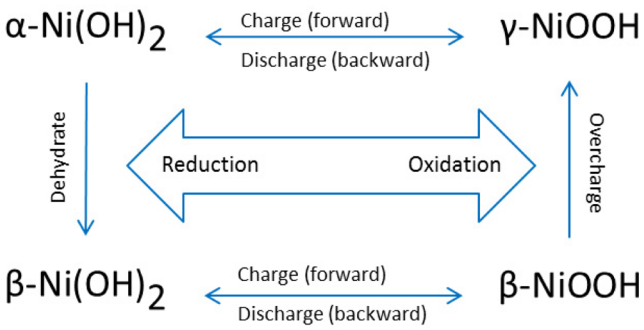

Figure 1. Four-phase Bode scheme of oxidation and reduction of $Ni(OH)_2$/NiOOH according to ref 27 as cited in ref 28.

hydrated form with intercalated water molecules is called α-$Ni(OH)_2$. In a highly concentrated alkaline solution, this structure is unstable and converts to the relatively anhydrous and thermodynamically stable polymorph β-$Ni(OH)_2$. The β-$Ni(OH)_2$ can then be charged to increase the oxidation state of Ni to about 3, which is called β-NiOOH. If it is further charged (overcharged), the β-NiOOH is converted to another polymorph, the so-called γ-NiOOH. There are several difficulties involved with the redox reaction between the β-phases, including volume expansion, which results in mechanical instability problems and a generally lower charge capacity.[29] Here, an alternative redox route is favorable where α-$Ni(OH)_2$ is directly oxidized to γ-NiOOH which can also occur at a lower potential than that required for the redox reaction between the two β-phases.[27] Another advantage of this route is that α-$Ni(OH)_2$ features a considerably lower mass density so that higher mass specific charge contents can be achieved. Hence, there is significant research dedicated to the stability enhancement of α-phase in alkaline milieus such as refs 29 and 30.

So far, very few attempts have been made to utilize $Ni(OH)_2$ film electrodes for microbattery applications. Humble et al. fabricated a Ni/Zn microbattery on an epoxy-coated silicone chip where the cathode consisted of a roughly 100 μm thick film deposited on a nickel current collector of around 600 nm in thickness. An estimation of the film electrodes characteristics resulted in an energy and power density of around 0.5 mW h cm^{-2} and 50 mW cm^{-2}, respectively.[31,32] Further research by Do et al. was concerned with the screen printing of $Ni(OH)_2$ thick film electrodes for Ni/MH batteries on porous ceramic substrates and on polypropylene films.[33,34] It is questionable whether or not this fabrication method can be easily adapted to microsystems. Additionally, such printed films have a limited tolerance for stress arising from volume change of the active materials[35] and from shear if in contact with flowing liquids as we may have in microfluidics.

In the present work, we report on a novel fabrication method for thin film electrodes of α-$Ni(OH)_2$ directly on glass, which is one of the most common microfluidic substrates. These electrodes can be employed for micropower applications such as rechargeable microbatteries or electrochemical capacitors. In contrast to the work of others, which are concerned with the electrodeposition of $Ni(OH)_2$ thin films on bulk nickel foils, such as refs 21 and 36, we use lithography techniques to create patterned films on the glass substrate. These microfabricated electrodes are characterized in terms of their material compositions and surface morphologies. We investigate the electrochemical performance of the patterned electrodes and compare them to similar but patternless film electrodes. This article continues with a section on the experimental methodologies and materials followed by a discussion of our experimental results. Finally, the article is summarized with some concluding remarks.

2. EXPERIMENTAL METHODS AND MATERIALS

In this section, we specify the materials, fabrication, and characterization techniques that are used for this work.

2.1. Microfabrication. *2.1.1. Materials.* Glass microscope slides (Fisher Scientific, Ottawa, ON, Canada) of area 1 × 3 square in. are used as the microfluidic substrate for the microfabrication of the $Ni(OH)_2$ films. Nickel and chromium pellets (Kurt J. Lesker Canada, Inc., Concord, ON, Canada) with purities of 99.995% and 99.998%, respectively, are used for the physical vapor deposition of the thin films. Electrodeposition is performed using nickel(II) chloride hexahydrate (puriss. p.a., >98%, Sigma-Aldrich Canada Company, Oakville, ON, Canada) and nickel(II) nitrate hexahydrate (99.999% trace metals basis, Sigma-Aldrich Canada Co.). Note that the use of a very high purity nickel nitrate solution is required since traces of coprecipitated metals such as iron can promote unwanted side reactions such as the oxygen evolution reaction (OER).[37] For the sake of comparison, nickel films are also prepared on nickel foil (99.99%, Sigma-Aldrich Canada Co.) with a thickness of 0.125 mm. The materials required for the ultraviolet (UV) lithography include a chemically amplified negative photoresist KMPR 1000, a SU-8 photoresist developer solution (methoxy-2-propanol acetate), and a photoresist remover PG solution (1-methylpyrrolidone) (all from MicroChem Corporation, Westborough, MA).

2.1.2. Instruments. Metal thin films are prepared using an electron beam evaporator (Thermionics Laboratory Inc., Hayward, CA) coupled with an IG4500 ion gauge controller. The deposition rate is controlled by a deposition crystal monitor (INFICON Inc., East Syracuse, NY). In terms of the UV lithography process, we use a glass photomask, with a grid-style geometric pattern consisting of squares of size 400 × 400 μm^2, obtained from nanoFAB at the University of Alberta (Edmonton, AB, Canada). The other photomask which is required for the patterning of the nickel current collector is made by printing on a regular office transparency sheet by using a XEROX office printer (XEROX WorkCentre 7428). A mask aligner (Oriel Instruments, Irvine, CA) coupled with a light intensity controller, timer, and UV lamp is used to transfer the mask pattern to the photoresist. In terms of electrodeposition, a power supply (U8002A, Agilent Technologies, Santa Clara, CA) along with a potentiostat/galvanostat (PGSTAT302N, Metrohm Autolab B.V., Utrecht, The Netherlands) are utilized.

2.2. Materials and Physical Characterization. The elemental composition of the deposited films is examined with an X-ray diffraction (XRD) instrument (X'Pert Pro, Philips Analytical B.V., Almelo, The Netherlands) via Cu Kα radiation. The diffractometer is operated at 40 kV and 45 mA. The data analysis is performed by using X'Pert Highscore Pro software. Additionally, we employ an X-ray photoelectron spectrometer (XPS) (Thermo Instruments, 310-F

DOI: 10.1021/acsami.5b01962
ACS Appl. Mater. Interfaces 2015, 7, 12797−12808

Microlab, Newburyport, MA, USA) using the Mg Kα method. A stylus profiler (Dektak XT, Bruker Nano Surfaces Division, Santa Barbara, CA, USA) is used to characterize the size features of the electrode surfaces. Furthermore, an infrared analysis is performed by using a Nicolet Avatar 320 Fourier transform infrared (FTIR) spectrometer (Thermo Fisher Scientific, Waltham, MA, USA) with a Specac Golden Gate single pass diamond attenuated total reflectance (ATR) accessory. A total number of 32 scans is collected at a resolution of 4 cm^{-1}.

2.3. Electrochemical Characterization. Electrode films are electrochemically characterized with cyclic voltammetry (CV), electrochemical impedance spectroscopy, and galvanostatic charge/discharge measurements using a potentiostat/galvanostat (PGSTAT302N, Metrohm Autolab B.V.). A three-electrode setup is utilized consisting of the working electrode ($Ni(OH)_2$), reference electrode (Ag/AgCl/3 M KCl, double junction, Metrohm Autolab B.V.), and a counter electrode (Pt wire mesh, Metrohm Autolab B.V.). All electrochemical measurements are performed in aqueous 1 M potassium hydroxide (KOH) solutions at a room temperature of 23 °C. The electrolyte solutions are prepared with deionized water having a conductivity of approximately 2 $\mu S\ cm^{-1}$. Conductivities and pH values are tested using a modular pH and conductivity meter (Mettler-Toledo, SevenMulti, Zurich, Switzerland). Additionally, a source measure unit instrument (2400-LV SourceMeter, Keithley Instruments Inc., Cleveland, OH) coupled with a four-probe station with Tungsten W probe tips (Wentworth Laboratories Inc., Brookfield, CT) is used to measure the surface resistance of the thin films.

3. RESULTS AND DISCUSSION

In this section, we first describe the microfabrication of the patterned film electrodes on glass substrates. These microfabricated electrodes are compared to similar patternless films which are deposited on commercially available nickel sheets.

3.1. Microfabrication. The $Ni(OH)_2$ thin film electrodes are made through microfabrication techniques which are commonly used in the semiconductor industry along with electroplating and electrodeposition. The process starts with the fabrication of a current collector on the microfluidic substrate using electron beam physical vapor deposition (e-beam evaporation). We first perform some qualitative experiments with sticky tape to test the adherence of the deposited thin films on glass. It turns out that pure nickel hardly adheres to glass. An improved adherence is achieved, when we first evaporate chromium to deposit an adhesion (seed) layer of a thickness of 40 nm on the glass surface. Then a nickel film of the same thickness is grown onto the adhesion layer. In terms of patternless electrodes, $Ni(OH)_2$ films are electrodeposited onto the current collector from the nickel nitrate solution in a potentiostatic mode. We observe that the durability of these $Ni(OH)_2$ films is very poor. Fu et al. used nickel sheet foils as the substrate for the electrodeposition of $Ni(OH)_2$ films.[21] They mentioned that the nickel foils were polished with emery paper to a rough finish. We use the same method for our electrode preparation on nickel foils since this enhances the adhesion with the film material, as we discuss in the next section. In our case, the very small thickness of the e-beam evaporative deposited current collectors prevents this kind of mechanical surface roughening. Therefore, we employ a novel approach which appears more suitable for microfabricated thin films. That is, we pattern the nickel current collector with a 3D array of micropillars. These 3D features not only simulate "roughness" of the surface, but also increase the size of the adhesion area.

The patterned electrode is fabricated through a multilayered film process which, along with e-beam evaporation and electroplating/electrodeposition, also employs multiple UV photolithography steps. The process steps are illustrated in Figure 2. In detail, the microscope glass slide is first subjected

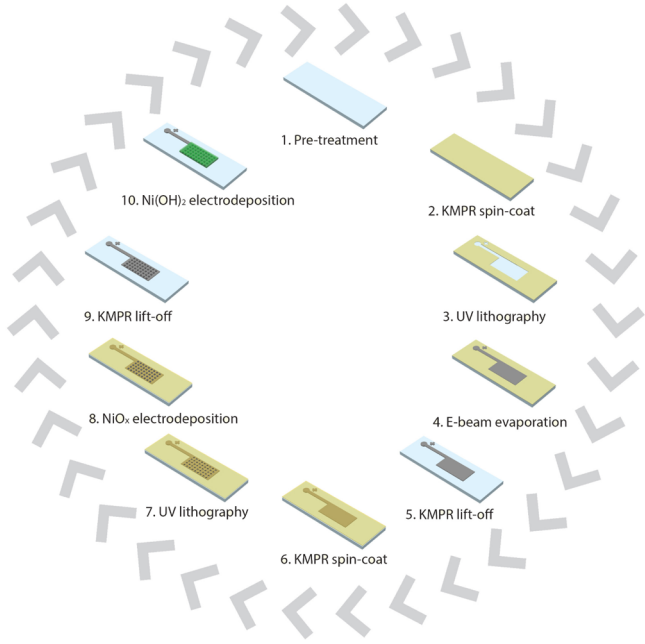

Figure 2. Fabrication process scheme of the patterned nickel hydroxide electrode.

to a cleaning process involving acetone, isopropanol, and deionized water. A layer of KMPR photoresist is spin-coated on the glass slide in two steps (500 rpm with an acceleration of 100 rpm s^{-1}, followed by 3000 rpm with an acceleration of 300 rpm s^{-1}). The slide with the photoresist is transferred to a hot plate and backed for 25 min at a temperature of 100 °C. To define the footprint of the electrode on the slide, the photoresist is exposed to UV light through the transparency sheet mask which initiates the cross-linking process. The exposure time is 6 s and the intensity controller reads 18.8 at a power of 1000 W. The glass slide is then transferred to the hot plate for a post exposure bake of 5 min at a temperature of 100 °C. The photoresist is developed in a SU-8 developer solution for about 5 min to remove the unexposed areas. That is, the unexposed bare glass surface area defines the location for the deposition of the current collector pad. The glass slide is transferred to the e-beam evaporation chamber where the chromium adhesion layer and subsequently the nickel current collector layer are grown; each film thickness is 40 nm. After deposition, the slide with the deposited metal layers is soaked in remover PG solution at a temperature of 60 °C to strip off the leftover photoresist. Note that soaking times of more than 20 min attack the nickel current collector severely, especially at elevated temperatures.

To create a patterned nickel surface, we process another layer of photoresist with the same fabrication parameters as described above. However, we use the photomask which patterns the photoresist with a grid of squares of size 400 × 400 μm^2. That is, we obtain a gridlike structure of alternating bare nickel and photoresist-coated squares after the lithography process. The microfabrication proceeds with the electroplating of nickel from a 1 M $NiCl_2$ solution for around 30 min at a potential of 0.9 V; the resulting current is $I \leq 0.01$ A. Since

DOI: 10.1021/acsami.5b01962
ACS Appl. Mater. Interfaces 2015, 7, 12797−12808

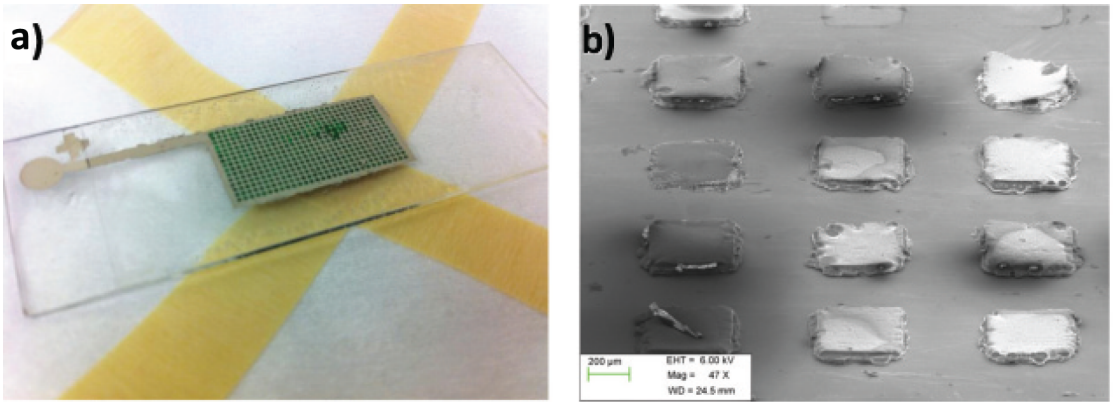

Figure 3. (a) Picture of the electrode current collector after electroplating of nickel which results in the three-dimensional gridlike pattern (the second photoresist layer is still present); (b) FESEM image of the electroplated nickel surface with a detailed view of the 3D features.

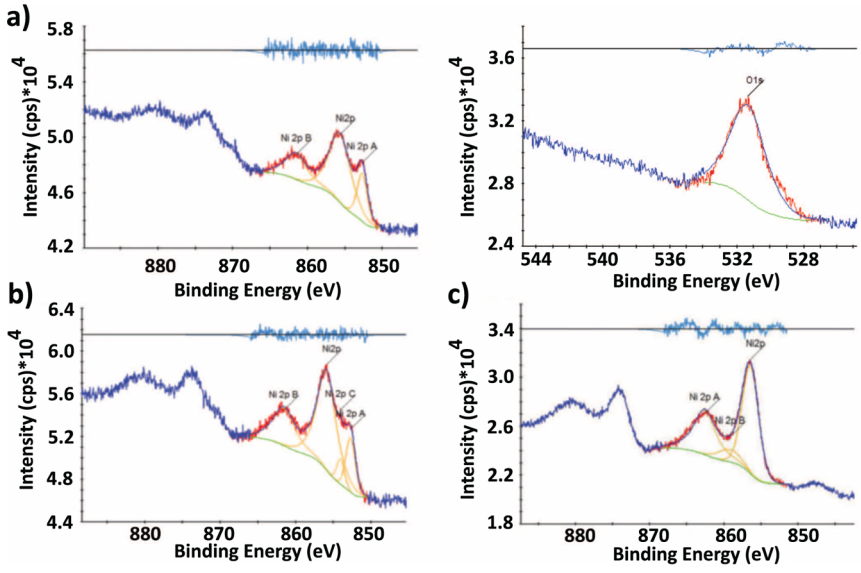

Figure 4. Ni(2p) spectrum from (a) a commercially available nickel sheet, (b) the e-beam evaporated nickel current collector, and (c) the electrodeposited nickel hydroxide film.

nickel is only deposited at the bare nickel surfaces of the current collector, a three-dimensional pattern of nickel micropillars is grown.

Once the three-dimensional features are fabricated, the remaining photoresist is stripped off the electrode pad using the same conditions as previously described. Finally, we grow a thin layer of $Ni(OH)_2$ from an aqueous $Ni(NO_3)_2{\cdot}6H_2O$ solution onto the entire electrode pad. According to ref 38, this electrodeposition process is based on the reduction of nitrate to ammonium via

$$NO_3^- + 7H_2O + 8e^- \rightarrow NH_4^+ + 10OH^- \quad (1)$$

The simultaneous generation of hydroxide raises the pH value at the cathode surface locally and the dissolved nickel ions react with the hydroxides and form insoluble nickel(II) hydroxides at the electrode surface according to

$$Ni^{2+} + 2OH^- \rightarrow Ni(OH)_2 \quad (2)$$

The electrodeposition is performed at a constant potential of −0.9 V vs Ag/AgCl for 30 min; the observed current density is around 3.25 mA cm^{-2}

Figure 3 gives insight into the structure of the electrode pad after different steps of the microfabrication process. In detail, Figure 3a shows a picture of the entire current collector after the electroplating of nickel, prior to stripping off the second photoresist layer and the electrodeposition of $Ni(OH)_2$. We notice the gridlike structure of the current collector which serves as an artificial surface roughness to improve the durability of the subsequently deposited $Ni(OH)_2$ film. Figure 3b shows a detailed 60° tilt field emission scanning electron microscopy (FESEM) image of the current collector surface, i.e., before the electrodeposition of $Ni(OH)_2$. The micropillars have, to good approximation, a footprint of 400 × 400 μm^2 and a distance of 400 μm between each other. The average height of a micropillar is determined to be around 20 μm by utilizing a (mechanical) stylus profiler. After the electrodeposition, the micropillars are covered by the $Ni(OH)_2$ layer with a thickness of around 35 μm. We observe that our patterning process significantly improves the stability of the films; the reason behind this is unknown. The gain in surface area is roughly 3%. This rather small change makes it less likely to be the cause of the stability improvement. An explanation could be the singularity of the electric field which results from sharp (ideal) geometric discontinuities. That is, there is a significant

DOI: 10.1021/acsami.5b01962
ACS Appl. Mater. Interfaces 2015, 7, 12797−12808

increase of the electric field strength at the edges and corners of the pillars which may result in a compacted electrodeposited film which improves mechanical strength and adhesion. In the next section, we discuss our results obtained from the materials characterizations and compare them with the relevant literature.

3.2. Materials Characterization. As outlined in the section Introduction, the electrochemical performance of $Ni(OH)_2$ is significantly affected by its crystal structure, grain size, and morphology. Hence, we employ several characterization methods to obtain insights into the composition, crystalline phase, and morphology of the substrates which are fabricated in this work. This detailed insight is especially important since we use multiple complex chemicals and methods for the film fabrications and we are not able to predict their impact on the substrates and the subsequent process steps.

We first utilize XPS measurements to investigate the surface composition of the different substrates. We follow Grosvenor et al.[39] in their interpretation on how the oxidation state of nickel at the surface is related to the binding energies and the chemical shifts in the XP spectra. In our study, the carbon offset is taken into account while the satellite peaks are not accounted for. Moreover, only the right-hand side set of peaks are used for the XP spectra interpretations and are fitted to the Ni(2p) multiplet.

In detail, Figure 4a shows the spectrum of the commercially available nickel sheet. This substrate is used to prepare a conventionally fabricated (patternless) $Ni(OH)_2$ electrode and is used as a benchmark for the microfabricated electrode. We observe two peaks at binding energies of 852.60 and 855.75 eV in the $Ni(2p_{3/2})$ spectrum, which correspond to Ni^0 and Ni^{2+}, respectively; the latter can be associated with the nickel in NiO.[39] Additionally, the right-hand side of Figure 4a shows another peak that is measured at 531.45 eV. This single O(1s) peak can reflect both OH^- and O^- or a Ni_2O_3 defect structure.[40] In comparison, Figure 4b shows the Ni(2p) multiplet peaks measured on the nickel film which is grown on glass using e-beam evaporation. The observed binding energies are 852.75 and 855.85 eV and, hence, are almost identical to those observed for the nickel sheet. However, the peak associated with Ni^0 is considerably less pronounced. Additionally, we measure an almost identical O(1s) peak (not shown) as for the nickel sheet. Generally, these results are in agreement with ref 39 and indicate that both substrates, nickel sheet and e-beam evaporated nickel film, have similar surfaces which consist of elemental nickel and nickel oxide. Considering the ratios of the $Ni(2p_{3/2})$ peaks, it appears that the e-beam evaporated film has a higher fraction of nickel oxide compared to the nickel sheet. Figure 4c shows the Ni(2p) spectrum of the $Ni(OH)_2$ film which is electrodeposited on the patterned current collector surface. We observe distinct peaks at 856.50 eV for $Ni(2p_{3/2})$ and 531.45 eV for O(1s) (not shown) which is similar to the nickel (and nickel oxide) surfaces discussed above. However, Kim and Winograd noted that this combination can also be assigned to $Ni(OH)_2$ since this spectrum is similar to that of Ni_2O_3 and NiO, except that the O(1s) peak is broader.[41] Finally, our XPS measurements confirm that, despite the multiple process steps and the usage of complex chemicals, the fabricated films consist of Ni^0 and Ni^{2+} bonded to an oxide or hydroxide compound, respectively.

Further information on the crystal phase and structure of the $Ni(OH)_2$ films are obtained by utilizing XRD technique. Here, we peel an electrodeposited film from a microfabricated electrode since powderlike samples are required. Figure 5 shows the measured XRD pattern which can be indexed

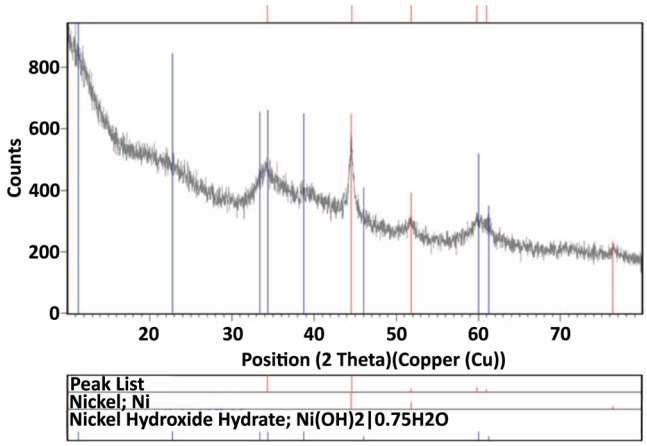

Figure 5. XRD pattern of the electrodeposited nickel hydroxide film.

according to JCPDS No. 38-0715 to the diffraction data of $Ni(OH)_2{\cdot}0.75H_2O$, i.e., to (hydrated) α-$Ni(OH)_2$. Similar patterns are observed in the work of others such as ref 21 who attributed the broadening of some of the diffraction peaks to small grain sizes or structural microdistortions in the crystal structure.

Finally, we perform FTIR-ATR spectroscopy of the electrodeposited $Ni(OH)_2$ films. The result gives a band which corresponds to a wavenumber of around 630 cm^{-1} (not shown). This can be attributed to the lattice vibration of hydroxyl groups (δNi−O−H) which is a typical feature of an α-$Ni(OH)_2$ structure.[21,42] Note that we are not able to obtain bands below 500 cm^{-1} by using our FTIR-ATR instrument. Therefore, the peaks which can be attributed to Ni−O stretching vibrations, as mentioned in refs 21 and 42 can not be found by using our instrument.

3.3. Electrochemical Characterization. In this section, we discuss the results of cyclic voltammetry, electrochemical impedance spectroscopy, charge/discharge measurements, and the durability of the differently fabricated $Ni(OH)_2$ film electrodes. Note that all electrochemical tests are performed in concentrated potassium hydroxide. Thus, the fabricated α-$Ni(OH)_2$ is dehydrated and converts into β-$Ni(OH)_2$.

3.3.1. Cyclic Voltammetry. Cyclic voltammetry is commonly used to identify both capacitive and faradic currents which result from the application of a cycling potential. In this section, we present cyclic voltammograms (CVs) of differently fabricated $Ni(OH)_2$ thin films that we term *conventional*, *patterned*, or *patternless* electrode. Here, the term conventional electrode means that the $Ni(OH)_2$ film is electrodeposited on a commercially available nickel sheet where the surface has been roughened with emery paper. The patterned and patternless electrodes are both deposited on glass and share most of the fabrication steps as described in subsection Microfabrication; however, one nickel surface is patterned with the micropillars while the other is plain. All CVs are measured in an aqueous 1 M KOH electrolyte. The measured currents are normalized with the footprint area of the electrode. We initially perform a few cycles at a scan rate of ν = 0.5 mV s^{-1} to condition the electrode. On average, around 20 cycles are required to obtain a steady and reproducible CV for the patterned or patternless

DOI: 10.1021/acsami.5b01962
ACS Appl. Mater. Interfaces 2015, 7, 12797−12808

electrodes while the conventional electrode requires fewer cycles for conditioning.

Figure 6 shows the CVs of the conventional electrode for different scan rates of ν = 0.5−15 mV s^{-1}. Note that we use an

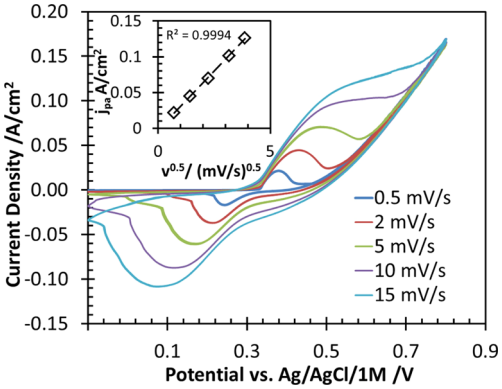

Figure 6. Cyclic voltammogram in 1 M KOH of a thin film of $Ni(OH)_2$ deposited on a nickel sheet for scan rates of ν = 0.5−15 mV s^{-1}. The insert demonstrates a linear correlation between the anodic current density and the square root of the scan rate.

IR-drop compensation of 75% for the measurements. Depending on the scan rate, we observe more or less distinct redox current peaks. That is, the higher the scan rate, the higher the magnitude of the measured current densities. Additionally, we observe a widening of the redox peaks with increasing scan rates. The redox peaks result from the electrochemical reaction between NiOOH and $Ni(OH)_2$ where Ni^{3+} is reduced to Ni^{2+} according to

$$\beta\text{-NiOOH} + H_2O + e^- \rightleftharpoons \beta\text{-Ni(OH)}_2 + OH^- \qquad E^{0\Theta} = 0.30\ \text{V(vs Ag/AgCl 3 M KCl)} \qquad (3)$$

In the following, we use the classic correlations and interpretations of cyclic voltammetry derived for smooth electrocatalytic electrodes as described for example in ref 43. It is understood that our $Ni(OH)_2$ films are porous substrates and not smooth surfaces and the redox reactions change the nature of the electrode surface as well. Nevertheless, since our porous films are very thin and the concentration gradients in the porous structure should be comparable to those on the surface, we think that this approach allows for a qualitative comparison. In other words, the aim of the interpretation is to quantify the variations of the differently fabricated electrodes rather than claiming the identification of the detailed electrochemical steps.

We observe that, for increasing scan rate, the anodic and cathodic peaks shift to higher and lower potentials, respectively. We plot the anodic current density values j_{pa} versus the square root of the scan rate $\sqrt{\nu}$ as shown in the inset of Figure 6. A clearly linear correlation between these parameters is observed. The average anodic peak potential corresponds to $\overline{E}_{pa}$ = 0.50 ± 0.11 V while the cathodic peak potential is found at $\overline{E}_{pc}$ = 0.16 ± 0.07 V. Hence, the average formal reduction potential corresponds to $\overline{E}^{o} = (\overline{E}_{pa} + \overline{E}_{pc})/2$ = 0.33 ± 0.02 V which is in good agreement with the standard reduction potential. We further find that the difference between the anodic and cathodic peak potentials increases in a linear fashion with $\sqrt{\nu}$. The average peak difference is with $\Delta\overline{E}_p$ = 0.34 ± 0.18 V rather large. The ratio of cathodic-to-anodic peak current distinctly decreases when the scan rate increases; the average value is $\overline{j}_{pc}/\overline{j}_{pa}$ = 0.47 ± 0.14. Considering all these features of the current CVs, it is indicated that there is an intrinsic activation barrier resulting in a slow electron transfer followed by a reversible chemical step; that is, the system is quasireversible.

The tails in the CVs displayed in Figure 6 at the highest oxidation potential indicates the presence of the parasitic OER. This mechanism is relatively complex and detailed investigations are outside of the scope of the present work; the reader is referred to ref 28 for further details on the OER in the presence of nickel. Snook et al. investigated the electrochemical performance of $Ni(OH)_2$ mixtures—consisting of $Ni(OH)_2$ particles, graphite flakes, and a PTFE binder—pasted on thick nickel foil collectors. They report that the OER diminishes the mechanical integrity of their electrodes and that cycling to a lower positive switching potential stabilizes the capacity and reduces the OER so that less electrode degradation occurs.[13] We observe that our thin film electrodes, which are without any binder, have a certain stability if deposited on the metal sheet, but are very much susceptible to mechanical degradation due to OER if they are fabricated onto the glass substrate. Additionally, the potential associated with the OER decreases as the scan rate decreases. To measure CVs of the electrodes deposited on glass, we adjust the switching potential for each scan rate such that we observe a distinct anodic peak while avoiding oxygen evolution as much as possible.

Figure 7a gives CVs of the patternless electrodes for scan rates of ν = 0.5−20 mV s^{-1}. Generally, we find distinct anodic and cathodic current peaks for all scan rates. We observe also

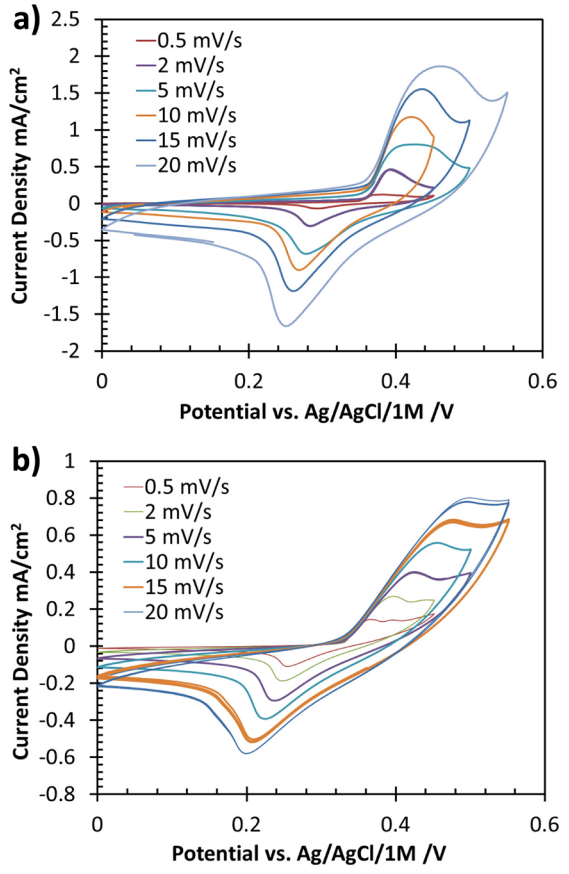

Figure 7. Cyclic voltammograms of the $Ni(OH)_2$ films at various scan rates for (a) the patternless and (b) the patterned electrodes.

DOI: 10.1021/acsami.5b01962
ACS Appl. Mater. Interfaces 2015, 7, 12797−12808

Table 1. Comparison of the Major CV Characteristics for the Differently Fabricated Electrodes

electrode	$\overline{E}^{o}$ (V)	$\Delta\overline{E}_p$ (V)	$\Delta E_p/\sqrt{\nu}$ (V s)$^{1/2}$	$j_{pa}/\sqrt{\nu}$ (A/(m^2 (V/s)$^{1/2}$))	j_{pc}/j_{pa}
conventional	0.33 ± 0.02	0.34 ± 0.18	0.229	10^{-4}	decreases with increasing ν
patternless	0.35 ± 0.01	0.16 ± 0.04	1.006	0.007	increases with increasing ν
patterned	0.33 ± 0.01	0.21 ± 0.07	0.652	0.019	increases with increasing ν

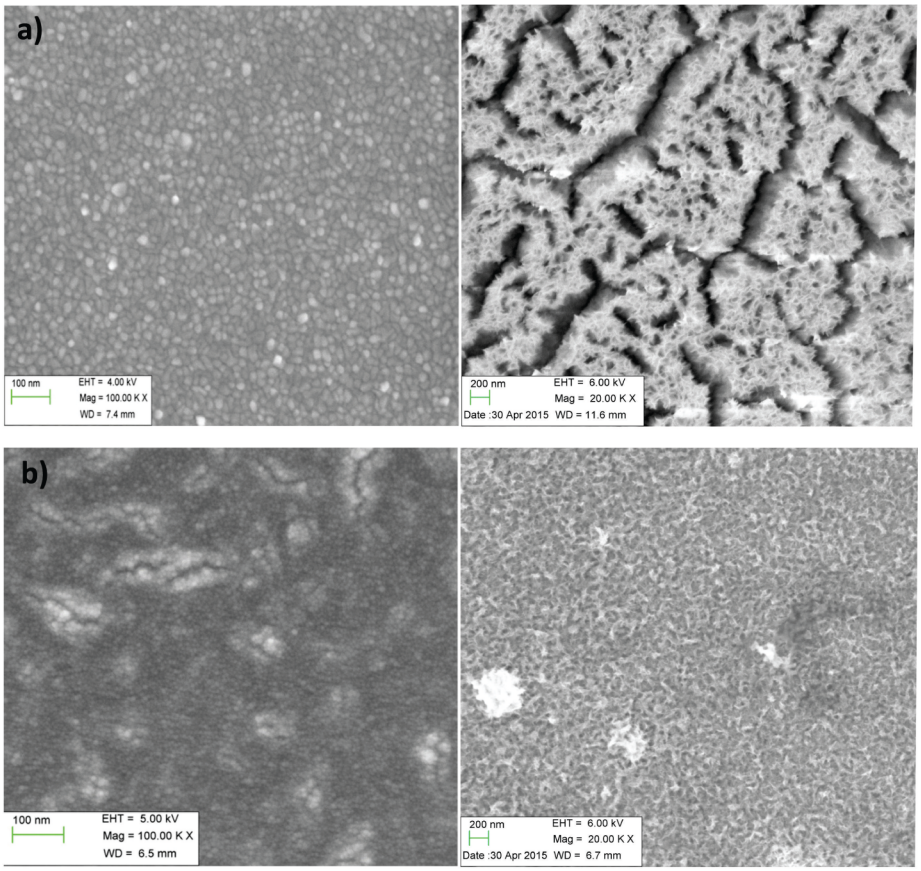

Figure 8. FESEM of current collector (left column) and electrodeposited $Ni(OH)_2$ film (right column) for (a) patternless electrode and (b) patterned electrode.

that the magnitude and the width of the peaks increases with increasing scan rate. Additionally, the anodic peak shifts to higher potentials and the cathodic peak shifts to lower potentials when we increase the scan rate. We determine the average anodic and cathodic peak potential to be $\overline{E}_{pa}$ = 0.43 ± 0.02 V and $\overline{E}_{pc}$ = 0.27 ± 0.01 V, respectively. The average peak difference over all scan rates is $\Delta\overline{E}_p$ = 0.16 ± 0.04 V while the average formal reduction potential corresponds to $\overline{E}^{o}$ = 0.35 ± 0.01 V. Further evaluation of the CVs shows again a linear correlation between anodic peak current and the square root of the scan rate. The average ratio of the peak currents is with $\overline{j}_{pc}/\overline{j}_{pa}$ = 0.47 ± 0.08, almost identical to that of the conventional electrode.

Figure 7b gives the CVs which are measured on the patterned electrode for various scan rates in a range of ν = 0.5−20 mV s^{-1} while the switching potentials are individually adjusted. We again realize that the magnitude and the width of the redox peaks increases with increasing scan rate. Additionally, we observe a noticeable distortion of the anodic peak for all scan rates. That is, the current density approaches its maximum and more or less maintains it until the switching potential is reached. Likewise to the previous electrodes, we observe that, with increasing scan rate, the difference between anodic and cathodic peaks increases. The average anodic peak potential corresponds to $\overline{E}_{pa}$ = 0.44 ± 0.05 V while the average cathodic potential is $\overline{E}_{pc}$ = 0.23 ± 0.02 V. Hence, the average peak difference over all scan rates is $\Delta\overline{E}_p$ = 0.21 ± 0.07 V. The average formal reduction potential corresponds to $\overline{E}^{o}$ = 0.33 ± 0.01 V. We again find that the anodic peak current scales linearly with the square root of the scan rate. The ratio of forward to backward peak current slightly increases with the scan rate; the average value is $\overline{j}_{pc}/\overline{j}_{pa}$ = 0.58 ± 0.05.

Table 1 summarizes the major findings obtained from the measurement of the CVs. All three electrodes share similar features such as the formal reduction potential and the linear relationship between the difference of the peak potentials and the square root of the scan rate. However, significant differences are observed in the dependency of the current peak ratio and the scan rate. For increasing scan rate, we observe a decrease for the conventional electrode but an increase for both microfabricated electrodes. In terms of the "classical" CV interpretation, these characteristics indicate that the microfabricated electrodes feature a slow electron transfer followed by an irreversible chemical step contrary to the reversible one which is identified for the conventional electrode. However, as already noted, we use the interpretation

DOI: 10.1021/acsami.5b01962
ACS Appl. Mater. Interfaces 2015, 7, 12797−12808

method only to describe the outcomes between the differently manufactured electrodes and do not claim that these are the real detailed mechanisms which occur. Additionally, the slope of the linear correlation between anodic peak current and square root of the scan rate is 1 order of magnitude smaller for the conventional electrode compared to those of the microfabricated electrodes. However, the material characterizations proved that the deposited films are equal in terms of composition despite the different electrode fabrication techniques. In conclusion, there is no obvious reason for these differences and the question arises whether these observations can be related to parameters other than the composition. Possible candidates are the variable turning potentials which may result in different concentration boundary layers at the electrodes, structural differences in the films, or the different current collectors that the films are deposited on, i.e., a thick nickel foil with low Ohmic resistance versus a very thin nickel layer on glass featuring a high resistance.

The difference between the anodic and cathodic peak potentials is a measure of the reversibility of the redox reactions. We find that the peak potential difference of the conventional electrode features the highest value while the patternless electrode has the lowest. That is, the reversibility of the microfabricated electrodes is better than that of the conventional one. Nevertheless, all electrodes that we measure indicate good reversibility behavior compared to respective literature data. Wang et al.[35] fabricated electrodes from spherical clusters of $Ni(OH)_2$ nanosheets which are grown onto a nickel foam current collector and report a high value of $\Delta E_p = 0.445$ V at a scan rate of 2 mV s^{-1}. Fu et al.[21] deposited $Ni(OH)_2$ films on a nickel foil, just like our conventional electrode, featuring similar values of $\Delta \bar{E}_p \approx 0.26$ V. Cai et al.[44] investigate $Ni(OH)_2$ mesoscale tubes and powders with measured peak potential differences of $\Delta \bar{E}_p = 0.12$ V and $\Delta \bar{E}_p = 0.18$ V, respectively.

Another important parameter is the potential difference between the anodic peak and the OER. The larger the difference, the longer the electrode can be charged below the potential where the OER occurs which allows for an enhanced utilization of the electroactive material.[45] We generally observe that the potential differences of the patternless electrodes are larger than those of the patterned electrodes. Nevertheless, during our experiments it turns out that the patterned electrodes show a much better durability than the patternless electrode, especially when we cycle with switching potentials close to the OER region. That is, the patterning of the nickel surface with micropillars results in an improved stability of the nickel hydroxide films.

Despite the better electrochemical reversibility data of the microfabricated electrodes, we observe a 1 order of magnitude lower peak current density compared to that of the conventional electrode at a given potential. Smaller, but still considerable, differences in peak current densities between both microfabricated electrodes are found as well; the patternless electrode's peak current densities are up to twofold of the respective value of the patterned one. We assume that this is related to the varying Ohmic resistances of the different current collectors and/or differences in the charge-transfer resistance due to structural differences.

Figure 8 gives insight into the surface morphology of the (a) patternless and the (b) patterned electrodes by FESEM pictures. Here, the left and right column shows the surface of the current collectors and the $Ni(OH)_2$ films, respectively. We recognize that the current collector surface of the patternless electrode consists of more or less homogeneously arranged grains, while the surface of the patterned electrode, even though mainly consisting of somewhat finer grains, appears rather irregular with cracks and larger "islands". Recall that the patterning of the electrode surface requires the lithography process with various complex chemicals, which we assume are responsible for the differences in the surface morphology. Interestingly, the situation is contrary to that of the electrodeposited films of $Ni(OH)_2$. That is, the surface of the patternless electrodes shows a coarse porous structure featuring many cracks despite the flawless current collector. Likewise, the patterned electrode has a finer homogeneous porous structure without cracks, although the current collector was inferior. Essentially, the different $Ni(OH)_2$ film surfaces may explain the behavior in terms of durability of the electrodes. That is, the many surface defects of the patternless electrode after the fabrication process are responsible for their limited life span.

To obtain a more quantitative statement, we employ the van der Pauw method[46] to determine the film (surface) resistance of the current collectors with a four-point probe station. Here, a small current is induced along an edge of the current collector while the potential is measured on the opposite edge. The film resistance R_f is then obtained from the correlation

$$\exp\left(-\frac{\pi R_A}{R_f}\right) + \exp\left(-\frac{\pi R_B}{R_f}\right) = 1 \tag{4}$$

where R_A and R_B are the resistances for both directions of the current collector calculated from Ohm's law in conjunction with the applied current and measured potential. Note that the van der Pauw method is originally concerned with the determination of the resistivity, which can be easily inferred from $\rho = R_f d$ if the film thickness d is known. We measure area-specific film resistances of around 1.38 and 2.08 Ω-cm^{-2} for patternless and patterned electrodes, respectively. Different protocols for the lithography steps of the patterned electrodes are pursued, but we always essentially observe the film resistances mentioned above. That is, the lithography steps create surfaces with considerably higher resistances compared to those of the plain current collector which does not come in contact with any of the chemicals used in the lithography step. The area-specific film resistance for the roughened nickel foil is measured to be 0.11 Ω-cm^{-2}. We realize that the ratios of the film resistances scale as the ratios of the peak current densities that we measure in the CVs.

We also measure the charge-transfer resistance and the capacitance of the differently fabricated film electrodes by employing EIS where we use the identical setup and conditioning as for the cyclic voltammetry measurements. In detail, EIS spectra are measured potentiostatically at a potential of 10 mV and in a frequency range of 0.01−100 kHz. We use this small potential to avoid any redox reaction during the impedance measurements. Otherwise, the electrode surface and the conversion degree would considerably change over the measurements at low frequencies. Figure 9 shows the results of the EIS measurements in form of a Nyquist plot. Because of the low excitation potential along with the high capacitance of the electrodes, only a limited segment of the typical semicircle is observed. The differences between patterned and patternless electrodes are obvious for lower frequencies. The spectra are fitted to an equivalent circuit which consists of the serial connection of the electrolyte resistance with the parallel

DOI: 10.1021/acsami.5b01962
ACS Appl. Mater. Interfaces 2015, 7, 12797−12808

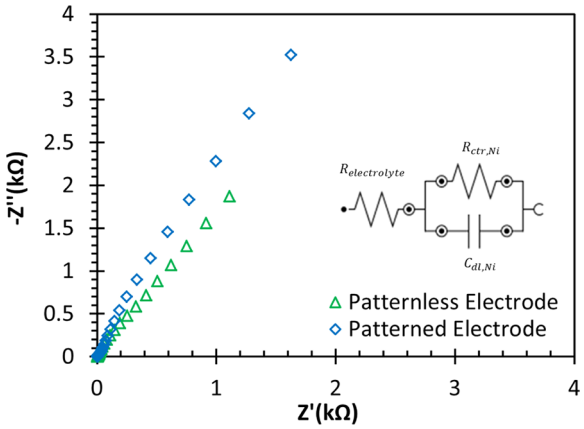

Figure 9. Nyquist plot of the patternless and the patterned electrodes.

arrangement of the electrode charge-transfer resistance and the electrode capacitance. The regression results in more or less identical capacitances of 1.85 and 2.15 mF for patterned and patternless electrodes, respectively. The difference in the charge-transfer resistances is more pronounced. The patternless electrode features a value of 1.53 kΩ while the patterned electrode is 4.22 kΩ. It should be noted that the Ohmic resistance of the current collector contributes to the charge-transfer resistance. The ratio of the charge-transfer resistances also corresponds approximately to the ratios of the peak current densities that we measure in the CVs. Hence, we conclude that the reason for the lower performance of the microfabricated electrodes in the CVs is due to the increased Ohmic resistance of the current collector along with a higher charge-transfer resistance. While we are not sure whether we can easily optimize the charge-transfer resistance of the film electrodes, it nevertheless appears promising to reduce the resistance of the current collector.

3.3.2. Charge and Discharge Characteristics. In this section, we examine charge and discharge characteristics of the three differently manufactured electrodes. Initially, all electrodes are preconditioned with cyclic voltammetry of low scan rates until a steady pattern is obtained; this usually takes around 20 cycles. In terms of the charge/discharge characteristics, we have to distinguish between the capacitance, which is the charge stored in the electrical double layer (EDL), and the (faradic) capacity which is related to the electrochemical conversion. The capacitance of $Ni(OH)_2$ is relatively high, and hence, these two phenomena can be relatively easily distinguished in the charge/discharge plots. In detail, after the regime has switched from charge to discharge, we observe that the potential remains similar to the charge potential for a certain time Δt_{EDL} before it sharply drops to negative values. The associated current is capacitive which means that we first discharge the double layers before the electrochemical reaction inverts the polarity of the potential.

It is important to mention that we cannot charge the electrodes to their highest states since the unavoidable potential increase triggers the OER, which compromises the mechanical integrity of the films; i.e., we cannot reliably measure the maximum capacity of the electrode films. Therefore, we estimate the theoretical capacity of the films to infer their state of charge (SOC), i.e., the ratio of the real amount of charge to that which can be theoretically stored. In detail, the electrochemical conversion occurs only at the surface of the porous thin films which is in contact with the electrolyte. Consequently, we assume that there is an electrochemically active layer of $Ni(OH)_2$ with a thickness corresponding to the mean grain size. We define a mass-specific electroactive volume $\overline{v}$, which is obtained from the product of BET surface area and the mean grain size of the $Ni(OH)_2$ film. We use a BET surface area of 62 $m^2\ g^{-1}$ as reported in ref 47. The mean grain size is estimated using the Scherrer equation (cf. ref48) while the required correlation parameters are obtained from the XRD measurements as described in subsection Materials Characterization. Note that this procedure is just an approximation due to the rather weak intensity of the XRD patterns. The electrochemically convertible mass of $Ni(OH)_2$ is then estimated by $V_{film}/\overline{v}$, where V_{film} is the (apparent) volume of the electrode, i.e., the electrode footprint area times the film thickness which is generally around 10 μm. Finally, the amount of charge which is required to convert the available material is calculated based on the stoichiometry of reaction 3. Note that in all calculations in this work a current efficiency of 100% is assumed.

At first, charge and discharge measurements of the conventional electrodes are investigated (results not shown). Since we cannot operate our microfabricated electrodes with charge/discharge current densities higher than j = 0.1 mA cm^{-2} without an immediate observation of electrode deterioration, we operate the conventional electrode with the same value to ensure comparability. The films are charged for 1000 min where we observe typical potentials of 0.30...0.35 V. Then, the films are discharged at the same current density for 1000 min to observe the electrode potential in the range of −0.30...−0.40 V. For these parameters, we observe that the film electrodes deposited on the nickel foil are relatively stable. The specific capacitance of the conventional electrode is estimated via $(I \times \Delta t_{EDL})/(\Delta V \times m)$, where I is the discharge current, Δt_{EDL} is the discharge time of the EDL, ΔV is the potential drop during the discharge time, and m is the mass of the $Ni(OH)_2$ film. On the basis of our experimental data, we calculate a specific capacitance of around 3000 F g^{-1}, which is in agreement with the work of Fu et al.[21] Additionally, we estimate the faradic capacity to be around 250 C g^{-1} (70 mA h g^{-1}), which corresponds to a SOC of around 25%. In comparison, Chen et al.[49] reported that their electrodes compacted from a mixture of Ni and $Ni(OH)_2$ powders feature a charge capacity of around 910 C g^{-1} (250 mA h g^{-1}) while the SOC is up to around 95%. Consequently, the comparison of our results to those of Chen et al. validates our method to estimate the electrochemically convertible mass of the films as outlined in the beginning of this section.

Figure 10 shows the charge/discharge characteristics of the patternless $Ni(OH)_2$ electrode at a current density of 0.1 mA cm^{-2}. In general, four stable cycles are observed before the first signs of film deterioration occur. The shape of the charge/discharge curves is more or less identical for all four cycles. During the charge and discharge process, the potential of the patternless electrode is around 0.32 and −1.04 V, respectively.

Figure 11 depicts the charge/discharge characteristics of the patterned electrode at a current density of 0.1 mA cm^{-2}. Typical charge and discharge potentials correspond to around 0.3 and −1 V, respectively, parameters which are similar to those of the patternless electrode. For these cycling conditions, we find no hint of electrode degradation even for a larger number of cycles. The capacity of the patternless and patterned electrodes are estimated to be around 140 and 70 mA h g^{-1},

DOI: 10.1021/acsami.5b01962
ACS Appl. Mater. Interfaces 2015, 7, 12797−12808

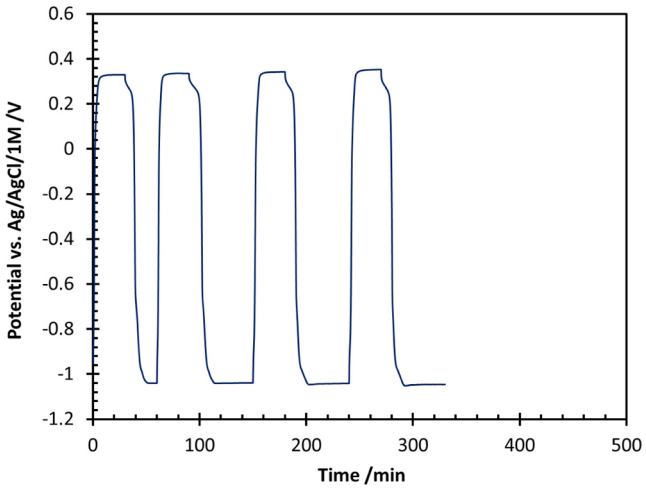

Figure 10. Charge and discharge behaviors of the patternless electrode at a constant current density of 0.1 mA cm^{-2}.

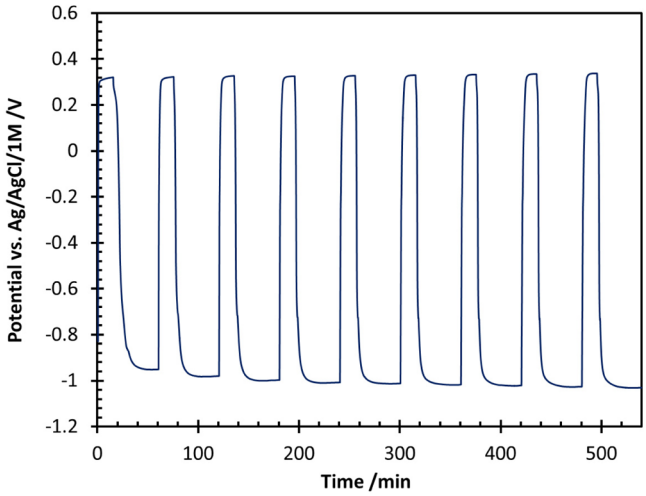

Figure 11. Charge and discharge behaviors of the patterned electrode at a current density of 0.1 mA cm^{-2}.

respectively. Then, the corresponding SOC of the electrode films are 50% and 25%, respectively

To enable a comparability of our results with those of Humble et al.,[31,32] who fabricated a roughly 100 μm thick patternless films on epoxy-coated silicon, we scale their capacity with the respective film thickness and arrive at 0.4 C mm^{-3}. The much thinner patternless and patterned electrodes fabricated on glass in this work feature 0.36 and 0.1 C mm^{-3}, respectively. We realize that we achieve similar values in terms of the patternless electrodes. In contrast, we do not observe the stability over a large number of cycles which is reported by Humble et al.; our patternless films last only very few cycles. An explanation could be, on the one hand, the different substrates (glass vs epoxy). On the other hand, there is an essential difference in the SOC. Humble et al. estimated a depth of discharge (DOD) of 10%, while the electroactive materials in our patternless films are, with a SOC of 50%, utilized much more heavily. Finally, our approach to pattern the electrode surfaces does result not only in stable films but also in an increased utilization (SOC of 25%) of the electroactive materials.

4. CONCLUSIONS

This study is concerned with the fabrication of nickel hydroxide thin film electrodes on glass substrates. A system which can be used, for instance, to realize integrated power sources on microfluidic devices. Indeed, we employ techniques which are commonly used for microfabrication along with electroplating and electrodeposition. We first utilize electron beam evaporation to deposit a chromium adhesion layer along with a nickel layer as the current collector on top of a glass surface. In the next step, nickel hydroxide films are electrodeposited onto the plane (patternless) current collector. We observe that the stability of these film electrodes is poor. Hence, we modify our film fabrication and include a lithography process to create a 3D array of micropillars onto the nickel current collectors. Extensive material characterization shows that, despite the utilization of multiple complex chemicals, patterned as well as patternless electrodes eventually consist of α-$Ni(OH)_2$. Cyclic voltammetry measurements of the patterned and the patternless electrodes on a glass substrate are performed and compared to comparable films deposited on a nickel sheet which serves as a benchmark case. The data that we measure indicate mainly similar electrochemical characteristics of all three electrode types, but the overall performance of the microfabricated electrodes on glass is inferior compared to those on the nickel sheet. Further investigations reveal that this can be assigned to the differences of the current collector film (surface) resistances and the charge-transfer resistances. Finally, the investigation of the charge/discharge characteristics demonstrates that patterning of the electrode surface on glass results in significantly higher durability compared to a patternless surface, especially in the presence of the parasitic oxygen evolution reaction. With respect to future research, further investigations on patterning mechanisms are desirable. Here, the influence of feature size, shape, and characteristic distance on the stability of the subsequently deposited electroactive films should be answered.

AUTHOR INFORMATION

Corresponding Author

*E-mail: dominik.barz@queensu.ca.

Notes

The authors declare no competing financial interest.

ACKNOWLEDGMENTS

The authors gratefully acknowledge the financial support from the Natural Sciences and Engineering Research Council of Canada (NSERC), the Canada Foundation for Innovation (CFI), and CMC microsystems. We also thank Dr. Wojtek Halliop, research scientist at Queen's–RMC Fuel Cell Research Centre, for useful discussion.

ABBREVIATIONS

ATR, attenuated total reflectance
CV, cyclic voltammogram
EIS, electrochemical impedance spectroscopy
FESEM, field emission scanning electron microscopy
FTIR, Fourier transform infrared
MEMS, micro-electro-mechanical systems
NiMH, nickel metal hydride
OER, oxygen evolution reaction
UV, ultraviolet
XRD, X-ray diffraction

DOI: 10.1021/acsami.5b01962
ACS Appl. Mater. Interfaces 2015, 7, 12797−12808

XPS, X-ray photoelectron spectroscopy

SUBSCRIPTS

pa,anodic peak
pc,cathodic peak

REFERENCES

(1) Jensen, K. F. Microreaction Engineering – Is Small Better? *Chem. Eng. Sci.* **2001**, *56*, 293–303.
(2) Abgrall, P.; Gué, A.-M. Lab-on-chip Technologies: Making a Microfluidic Network and Coupling it into a Complete Microsystem - A Review. *J. Micromech. Microeng.* **2007**, *17*, R15.
(3) Gervais, L.; De Rooij, N.; Delamarche, E. Microfluidic Chips for Point-of-Care Immunodiagnostics. *Adv. Mater.* **2011**, *23*, H151–H176.
(4) Arthur, T. S.; Bates, D. J.; Cirigliano, N.; Johnson, D. C.; Malati, P.; Mosby, J. M.; Perre, E.; Rawls, M. T.; Prieto, A. L.; Dunn, B. Three-dimensional Electrodes and Battery Architectures. *MRS Bull.* **2011**, *36*, 523–531.
(5) Souquet, J. L.; Duclot, M. Thin Film Lithium Batteries. *Solid State Ionics* **2002**, *148*, 375–379.
(6) Zhu, L.; Kim, D.; Kim, H.; Masel, R.; Shannon, M. Hydrogen Generation from Hydrides in Millimeter Scale Reactors for Micro Proton Exchange Membrane Fuel Cell Applications. *J. Power Sources* **2008**, *185*, 1334–1339.
(7) Cook-Chennault, K. A.; Thambi, N.; Sastry, A. M. Powering MEMS Portable Devices-A Review of Non-Regenerative and Regenerative Power Supply Systems with Special Emphasis on Piezoelectric Energy Harvesting Systems. *Smart Mater. Struct.* **2008**, *17*, 043001.
(8) Yang, Y.; Liu, J. Micro/Nanofluidics-Enabled Energy Conversion and its Implemented Devices. *Front. Energy* **2011**, *5*, 270–287.
(9) Kundu, A.; Jang, J.; Gil, J.; Jung, C.; Lee, H.; Kim, S.-H.; Ku, B.; Oh, Y. Micro-Fuel Cells – Current Development and Applications. *J. Power Sources* **2007**, *170*, 67–78.
(10) Kjeang, E.; Djilali, N.; Sinton, D. Microfluidic Fuel Cells: A Review. *J. Power Sources* **2009**, *186*, 353–369.
(11) Ho, C. C.; Evans, J. W.; Wright, P. K. Direct Write Dispenser Printing of a Zinc Microbattery with an Ionic Liquid Gel Electrolyte. *J. Micromech. Microeng.* **2010**, *20*, 104009.
(12) Oudenhoven, J.; Vullers, R.; Schaijk, R. A Review of the Present Situation and Future Developments of Micro-Batteries for Wireless Autonomous Sensor Systems. *Int. J. Energy Res.* **2012**, *36*, 1139–1150.
(13) Snook, G. A.; Duffy, N. W.; Pandolfo, A. G. Evaluation of the Effects of Oxygen Evolution on the Capacity and Cycle Life of Nickel Hydroxide Electrode Materials. *J. Power Sources* **2007**, *168*, 513–521.
(14) Ahlberg, E.; Palmqvist, U.; Simic, N.; Sjövall, R. Capacity Loss in Ni-Cd Pocket Plate Batteries. The Origin of the Second Voltage Plateau. *J. Power Sources* **2000**, *85*, 245–253.
(15) McLarnon, F. R.; Cairns, E. J. The Secondary Alkaline Zinc Electrode. *J. Electrochem. Soc.* **1991**, *138*, 645–656.
(16) Do Jin, J.; Woo-Seong, K.; Sung, Y.-E. Improved Electrochromic Response Time of Nickel Hydroxide Thin Film by Ultra-Thin Nickel Metal Layer. *Jpn. J. Appl. Phys.* **2001**, *40*, L708–L710.
(17) Carpenter, M.; Corrigan, D. Photoelectrochemistry of Nickel Hydroxide Thin Films. *J. Electrochem. Soc.* **1989**, *136*, 1022–1026.
(18) Kalu, E.; Nwoga, T.; Srinivasan, V.; Weidner, J. Cyclic Voltammetric Studies of the Effects of Time and Temperature on the Capacitance of Electrochemically Deposited Nickel Hydroxide. *J. Power Sources* **2001**, *92*, 163–167.
(19) Zhao, D.-D.; Bao, S.-J.; Zhou, W.-J.; Li, H.-L. Preparation of Hexagonal Nanoporous Nickel Hydroxide Film and its Application for Electrochemical Capacitor. *Electrochem. Commun.* **2007**, *9*, 869–874.
(20) Wu, M.-S.; Huang, Y.-A.; Yang, C.-H. Capacitive Behavior of Porous Nickel Oxide/Hydroxide Electrodes with Interconnected Nanoflakes Synthesized by Anodic Electrodeposition. *J. Electrochem. Soc.* **2008**, *155*, A798–A805.
(21) Fu, G.; Hu, Z.; Xie, L.; Jin, X.; Xie, Y.; Wang, Y.; Zhang, Z.; Yang, Y.; Wu, H. Electrodeposition of Nickel Hydroxide Films on Nickel Foil and its Electrochemical Performances for Supercapacitor. *Int. J. Electrochem. Sci.* **2009**, *4*, 1052–1062.
(22) Dubal, D. P.; Gund, G. S.; Lokhande, C. D.; Holze, R. Decoration of Spongelike $Ni(OH)_2$ Nanoparticles onto MWCNTs Using an Easily Manipulated Chemical Protocol for Supercapacitors. *ACS Appl. Mater. Interfaces* **2013**, *5*, 2446–2454.
(23) Chen, H.; Cai, F.; Kang, Y.; Zeng, S.; Chen, M.; Li, Q. Facile Assembly of Ni-Co Hydroxide Nanoflakes on Carbon Nanotube Network with Highly Electrochemical Capacitive Performance. *ACS Appl. Mater. Interfaces* **2014**, *6*, 19630–19637.
(24) Wu, L. C.; Chen, Y. J.; Mao, M. L.; Li, Q. H.; Zhang, M. Facile Synthesis of Spike-Piece-Structured $Ni(OH)_2$ Interlayer Nanoplates on Nickel Foam as Advanced Pseudocapacitive Materials for Energy Storage. *ACS Appl. Mater. Interfaces* **2014**, *6*, 5168–5174.
(25) Du, H.; Jiao, L.; Cao, K.; Wang, Y.; Yuan, H. Polyol-Mediated Synthesis of Mesoporous α-$Ni(OH)_2$ with Enhanced Supercapacitance. *ACS Appl. Mater. Interfaces* **2013**, *5*, 6643–6648.
(26) Han, G.-F.; Xiao, B.-B.; Lang, X.-Y.; Wen, Z.; Zhu, Y.-F.; Zhao, M.; Li, J.-C.; Jiang, Q. Self-grown $Ni(OH)_2$ Layer on Bimodal Nanoporous AuNi Alloys for Enhanced Electrocatalytic Activity and Stability. *ACS Appl. Mater. Interfaces* **2014**, *6*, 16966–16973.
(27) Bode, H.; Dehmelt, K.; Witte, J. Zur Kenntnis der Nickelhydroxidelektrode–I. Über das Nickel(II)-hydroxidhydrat. *Electrochim. Acta* **1966**, *11*, 1079–1087.
(28) Lyons, M. E.; Brandon, M. P. The Oxygen Evolution Reaction on Passive Oxide Covered Transition Metal Electrodes in Aqueous Alkaline Solution Part 1-Nickel. *Int. J. Electrochem. Sci.* **2008**, *3*, 1386–1424.
(29) Zhao, Y.; Wang, J.; Chen, H.; Pan, T.; Zhang, J.; Cao, C. Different Additives-Substituted α-Nickel Hydroxide Prepared by Urea Decomposition. *Electrochim. Acta* **2004**, *50*, 91–98.
(30) Hu, W.-K.; Noréus, D. Alpha Nickel Hydroxides as Lightweight Nickel Electrode Materials for Alkaline Rechargeable Cells. *Chem. Mater.* **2003**, *15*, 974–978.
(31) Humble, P. H.; Harb, J. N.; LaFollette, R. Microscopic Nickel-Zinc Batteries for Use in Autonomous Microsystems. *J. Electrochem. Soc.* **2001**, *148*, A1357–A1361.
(32) Humble, P. H.; Harb, J. N. Optimization of Nickel-Zinc Microbatteries for Hybrid Powered Microsensor Systems. *J. Electrochem. Soc.* **2003**, *150*, A1182–A1187.
(33) Do, J.-S.; Yu, S.-H.; Cheng, S.-F. Thick-Film Nickel-Metal-Hydride Battery Based on Porous Ceramic Substrates. *J. Power Sources* **2003**, *117*, 203–211.
(34) Do, J.-S.; Yu, S.-H.; Cheng, S.-F. Preparation and Characterization of Thick-Film Ni/MH Battery. *Biosens. Bioelectron.* **2004**, *20*, 61–67.
(35) Wang, Y.; Cao, D.; Wang, G.; Wang, S.; Wen, J.; Yin, J. Spherical Clusters of β-$Ni(OH)_2$ Nanosheets Supported on Nickel Foam for Nickel Metal Hydride Battery. *Electrochim. Acta* **2011**, *56*, 8285–8290.
(36) Lyons, M. E.; Cakara, A.; O'Brien, P.; Godwin, I.; Doyle, R. L. Redox, pH sensing and Electrolytic Water Splitting Properties of Electrochemically Generated Nickel Hydroxide Thin Films in Aqueous Alkaline Solution. *Int. J. Electrochem. Sci.* **2012**, *7*, 11768–11795.
(37) Corrigan, D. A. The Catalysis of the Oxygen Evolution Reaction by Iron Impurities in Thin Film Nickel Oxide Electrodes. *J. Electrochem. Soc.* **1987**, *134*, 377–384.
(38) Corrigan, D. A.; Bendert, R. M. Effect of Coprecipitated Metal Ions on the Electrochemistry of Nickel Hydroxide Thin Films: Cyclic Voltammetry in 1M KOH. *J. Electrochem. Soc.* **1989**, *136*, 723–728.
(39) Grosvenor, A. P.; Biesinger, M. C.; Smart, R. S.; McIntyre, N. S. New Interpretations of XPS Spectra of Nickel Metal and Oxides. *Surf. Sci.* **2006**, *600*, 1771–1779.
(40) Moroney, L. M.; Smart, R. S. C.; Roberts, M. W. Studies of the Thermal Decomposition of βNiO(OH) and Nickel Peroxide by X-ray Photoelectron Spectroscopy. *J. Chem. Soc., Faraday Trans. 1* **1983**, *79*, 1769–1778.
(41) Kim, K.; Winograd, N. X-ray Photoelectron Spectroscopic Studies of Nickel-Oxygen Surfaces using Oxygen and Argon Ion-Bombardment. *Surf. Sci.* **1974**, *43*, 625–643.

DOI: 10.1021/acsami.5b01962
ACS Appl. Mater. Interfaces 2015, 7, 12797–12808

(42) Kamath, P.; Subbanna, G. Electroless Nickel Hydroxide: Synthesis and Characterization. *J. Appl. Electrochem.* **1992**, *22*, 478−482.
(43) Hamann, C.; Hamnett, A.; Vielstich, W. *Electrochemistry*; Wiley-VCH: New York, 2007.
(44) Cai, F.-S.; Zhang, G.-Y.; Chen, J.; Gou, X.-L.; Liu, H.-K.; Dou, S.-X. $Ni(OH)_2$ Tubes with Mesoscale Dimensions as Positive-Electrode Materials of Alkaline Rechargeable Batteries. *Angew. Chem., Int. Ed.* **2004**, *43*, 4212−4216.
(45) Li, W.; Zhang, S.; Chen, J. Synthesis, Characterization, and Electrochemical Application of $Ca(OH)_2$-, $Co(OH)_2$-, and $Y(OH)_3$-Coated $Ni(OH)_2$ Tubes. *J. Phys. Chem. B* **2005**, *109*, 14025−14032.
(46) van der Pauw, L. A Method of Measuring Specific Resistivity and Hall effect of Discs of Arbitrary Shape. *Philips Res. Rep.* **1958**, *13*, 1−9.
(47) Wang, D.; Song, C.; Hu, Z.; Fu, X. Fabrication of Hollow Spheres and Thin Films of Nickel Hydroxide and Nickel Oxide with Hierarchical Structures. *J. Phys. Chem. B* **2005**, *109*, 1125−1129.
(48) Jones, F. W. The Measurement of Particle Size by the X-Ray Method. *Proc. R. Soc. London, Ser. A* **1938**, *166*, 16−43.
(49) Chen, J.; Bradhurst, D. H.; Dou, S. X.; Liu, H. K. Nickel Hydroxide as an Active Material for the Positive Electrode in Rechargeable Alkaline Batteries. *J. Electrochem. Soc.* **1999**, *146*, 3606−3612.

DOI: 10.1021/acsami.5b01962
ACS Appl. Mater. Interfaces 2015, 7, 12797−12808